Review

Ion Irradiation for Planar Patterning of Magnetic Materials

Takeshi Kato [1,*] , **Daiki Oshima** [2] and **Satoshi Iwata** [2]

1   Department of Electronics, Nagoya University Furo-cho, Chikusa-ku, Nagoya 464-8603, Japan
2   Institute of Materials and Systems for Sustainability, Nagoya University Furo-cho, Chikusa-ku, Nagoya 464-8603, Japan; oshima.daiki@a.mbox.nagoya-u.ac.jp (D.O.); iwata.satoshi@k.mbox.nagoya-u.ac.jp (S.I.)
*   Correspondence: kato.takeshi@b.mbox.nagoya-u.ac.jp

Abstract: Kr^+ ion dose dependence of the magnetic properties of MnGa films and the fabrication of planar-patterned MnGa films by the local ion irradiation technique were reviewed. The magnetization and perpendicular anisotropy of the MnGa vanished at an ion dose of 1×10^{14} ions/cm^2 due to the phase change of the MnGa from ferromagnetic L1$_0$ to paramagnetic A1 phase. The average switching field H_{sw} of the planar-patterned MnGa increased with decreasing the bit size, implying low bit edge damage in the patterned MnGa, whereas a rather large switching field distribution (SFD) of 25% was confirmed for a bit size of ~40 nm. Time resolved magneto-optical Kerr effect measurements revealed that as-prepared MnGa exhibits an effective anisotropy field $H_{keff} = 20$ kOe, its distribution $\Delta H_{keff} = 200$ Oe, and Gilbert damping $\alpha = 0.008$. The ion-irradiated MnGa films exhibited larger $H_{keff} = 22$–23 kOe than that of the MnGa before the ion dose. Thus, ion irradiation does not decrease the perpendicular anisotropy, which suggests a small bit edge in the patterned MnGa. ΔH_{keff} increased from 0.2 kOe to 3 kOe, whereas the length of disorder in the film ξ decreased from 10 nm to 3 nm by ion irradiation.

Keywords: ion irradiation; bit patterned media; magnetic recording; phase change; surface flatness

1. Introduction

The nanofabrication of magnetic materials is quite important technology for achieving increased magnetic storage and memory capacities, as well as improved performance of magnetic sensors. For magnetic storage, nano-structured magnetic heads fly a few nanometers above the storage media in the hard disk drive (HDD) to pick up the nano-scale magnetic flux change on the medium surface. The nano-sized magnetic patterning on the storage media, referred to as bit patterned media (BPM), is known as a potential way to increase the density of HDDs [1–3]. BPM provide a promising approach to postpone the problem of the superparamagnetic limit [4], i.e., the thermal instability of recorded bits. Conventional granular media are faced with this problem, which limits the recording density of the HDD up to 1 Tb/in^2 [5].

In BPM, a periodic array of magnetic nano-dots is defined lithographically on the disk. The period of the nano-dots array is estimated to be 18 nm to realize 2 Tb/in^2 [2]. The nano-dots must have small fluctuations of dot positions and sizes as well as a small switching field distribution (SFD). These fluctuations are considered to be less than 10% [2]. BPM should also have a smooth disk surface with roughness less than ~1 nm, for the flyability of the head [6]. Most importantly, BPM are fabricated at low cost on a large scale.

Ion irradiation to the magnetic film allows magnetic patterning without modifying the surface roughness of the film. BPM fabrication by ion irradiation thus does not require surface-flattening

processes, such as trench filling and polishing, which are required for the conventional ion etching process to make the medium surface sufficiently flat for the stable flying of the recording head. The flattening processes are major problems in BPM fabrication, since they make the medium cost high and the fabrication yield low.

In 1998, Chappert et al. reported their first study of ion irradiation into Co/Pt multilayers and they demonstrated so-called planar BPM fabricated by local ion irradiation [7]. Later, ion irradiation to Co/Pt [8,9] and Co/Pd [10,11] was studied to discuss the mechanism of the magnetic patterning and the ultimate limit of the density of planar BPM. In such materials, ion irradiation changes their magnetization easy axis from the film normal to the film plane due to the intermixing between Co and noble metal layers at the interface, and planar BPM with bit sizes down to a sub-micron scale have been reported [7]. Since the perpendicularly magnetized bits are separated by the in-plane magnetized region, the adjacent bits magnetically couple through exchange coupling, which will limit the ultimate density of the BPM [11]. In order to overcome this problem, materials whose magnetism is modified, i.e., from ferromagnetic to paramagnetic, by ion irradiation are desired. The magnetizations of CoCrPt [12] and FePt [13] were reported to be reduced by ion implantation, however a quite high ion dose of 10^{15}–10^{16} ions/cm^2 is required to reduce their magnetizations. There are other reports of ion irradiation into FeAl, where the antiferromagnetic B2 phase was changed to the ferromagnetic A2 phase by an ion dose of less than 10^{15} ions/cm^2 [14].

We reported that 30 keV Kr$^+$ ion implantation altered the magnetism of CrPt$_3$ [15–18], MnAl [19], MnGa [19–22], and MnBiCu [23] from ferromagnetic to paramagnetic according to the change of the crystal structure from the ordered to disordered phase. All of these materials exhibit a strong perpendicular magnetic anisotropy, which is an essential property for high-density BPM. In these materials, a quite low ion dose ~10^{14} ions/cm^2 is sufficient to change their magnetism. We also demonstrated high-density planar BPM with a period of the bit array down to 80 nm [20,22] and HDD head flyable planar BPM by using this technique [15]. We observed that the SFD of the ion beam-patterned MnGa was ~25% [22], and discussed the origins of the SFD. In this article, we first review the results of ion irradiation into MnGa presented in our previous papers [20–22], and report the magnetization dynamics of the irradiated MnGa films to determine the origin of SFD in more detail.

2. Control of the Structure and Magnetic Properties of MnGa Films by Ion Implantation

In a Mn$_x$Ga$_{100-x}$ alloy system, L1$_0$ ordered phase is known to be stable for $x = 0.5$–0.65, and D0$_{22}$ phase is known to be stable for $x = 0.65$–0.75. The L1$_0$ and D0$_{22}$ MnGa films exhibit strong perpendicular magnetic anisotropy when the films were grown with (001) orientation [24]. Figure 1 shows *M-H* loops of MnGa films (a) before and (b) after the irradiation measured by an alternating gradient field magnetometer (AGM). The MnGa films were grown on MgO(001) substrate with (001)-oriented Cr (20 nm) buffer layer by the co-sputtering of Mn$_{40}$Ga$_{60}$ and Mn$_{60}$Ga$_{40}$ targets at 300 °C, and subsequently annealed at 400 °C. Then, 30 keV Kr$^+$ ions were irradiated to the as-prepared MnGa to control the structure and magnetic properties of the MnGa film. The saturation magnetization M_s and effective anisotropy field H_{keff} of the L1$_0$-MnGa film are estimated to be M_s ~450 emu/cc and H_{keff} ~25 kOe, respectively. After the ion dose at 1×10^{14} ions/cm^2, the ferromagnetism of the MnGa film disappeared (Figure 1b). Figure 2 shows the X-ray diffraction (XRD) profiles of the MnGa films before and after ion irradiation. In the profile before the irradiation, Cr and MnGa 002 peaks were clearly confirmed, indicating that the MnGa film has a (001)-oriented structure. Moreover, 001 MnGa superlattice peak indicates the formation of the ferromagnetic L1$_0$ ordered phase as shown in Figure 2. With an increase in the ion dose, the MnGa 001 peak decreased and the 002 peak shifted toward a lower angle. This indicates the phase change from the ferromagnetic L1$_0$ ordered phase to a paramagnetic A1 disordered phase by the ion irradiation as shown in Figure 2 (see also Refs. [20,22]). The variation of the XRD profiles explains well the change of the magnetic properties. The MnGa film exhibited a strong perpendicular magnetic anisotropy as shown in Figure 1a, since the MnGa film had a (001)-oriented L1$_0$ ordered structure before the irradiation. The ion irradiation at 1×10^{14} ions/cm^2

completely changed the crystal structure to an A1 disordered phase, which makes the magnetism of the film paramagnetic as shown in Figure 1b.
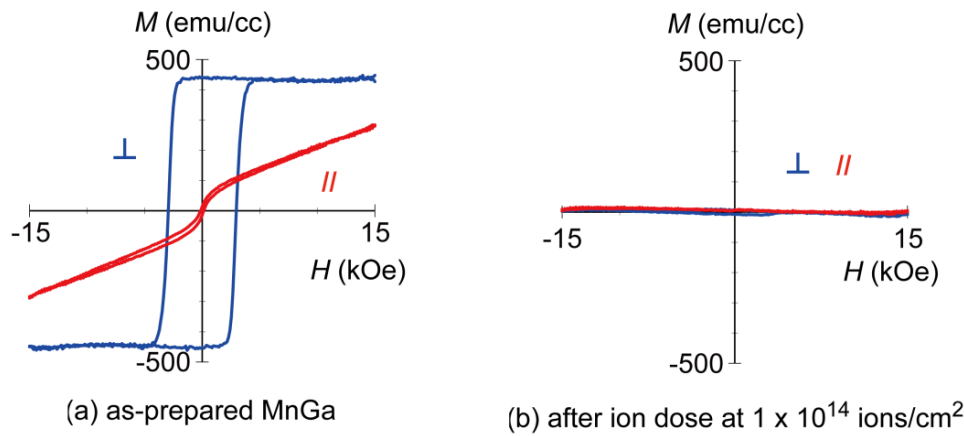

Figure 1. *M-H* loops of MnGa films (**a**) before and (**b**) after the ion dose at 1×10^{14} ions/cm². The loops were taken applying a magnetic field parallel or perpendicular to the film plane [20].
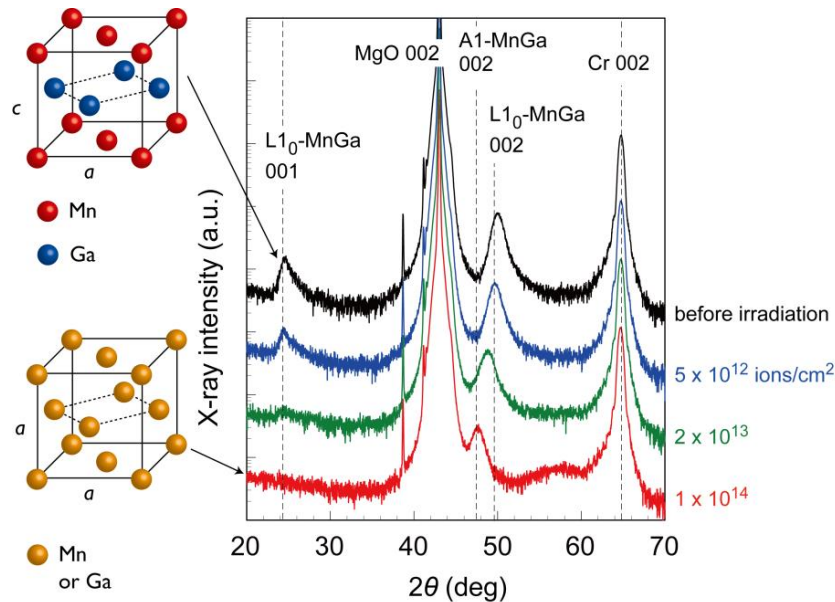

Figure 2. X-ray diffraction profiles of MnGa films before and after Kr$^+$ ion irradiation. The crystal structures of L1$_0$ ordered and A1 disordered phases are also shown.

Figure 3 illustrates the 30 keV Kr$^+$ ion dose dependences of the saturation magnetization M_s, coercivity H_c, and perpendicular anisotropy K_u of the MnGa films. These values were normalized as the values before the irradiation to be 1. M_s and K_u gradually decreased with increasing ion dose, whereas H_c increased slightly at the low ion dose up to 10^{13} ions/cm² and then decreased with the increase in the ion dose. One can observe that K_u of the MnGa decreased in proportion to M_s. This implies that the reduction of M_s by the ion implantation is not caused by the decrease of the Curie temperature T_C of the MnGa. The temperature dependence of K_u is known to be proportional to $M_s^2 \sim M_s^3$, and thus if the ion irradiation causes the reduction of T_C, K_u should decrease in proportion to $M_s^2 \sim M_s^3$ [25,26]. Figure 4 shows the ion dose dependence of T_C and M_s of MnGa films. As expected from the ion dose dependence of M_s and K_u shown in Figure 3, T_C did not decrease up to the ion dose of 10^{13} ions/cm². Based on these results, the microstructure of the ion-implanted MnGa is expected to be a mixture of the ferromagnetic L1$_0$-MnGa and paramagnetic A1-MnGa illustrated in Figure 3. The increase of H_c up to 10^{13} ions/cm² in Figure 3 and the decrease of T_C at 2×10^{14} ions/cm² in

Figure 4 are also explained by this microstructure. The ion dose of 10^{13} ions/cm^2 corresponds to one ion per 3 nm $\times$ 3 nm square. We speculate that such an ion dose creates local nonmagnetic A1-MnGa regions which act as pinning centers to impede the smooth propagation of the domain wall, resulting in the increase of H_c. The gradual change of XRD profiles with the ion dose shown in Figure 2 is also explained by the microstructure shown in Figure 3, since the coherent length of the X-ray is much longer than the lateral size of the microstructure. The increase of the ion dose will increase the volume ratio of the A1 phase/L1$_0$ phase, and then the L1$_0$ MnGa nano-crystals will be surrounded by the paramagnetic A1 MnGa matrix. The L1$_0$-MnGa nano-crystal exhibits low H_c and T_C compared to those of the L1$_0$-MnGa film due to the thermal fluctuation of the magnetization at room temperature. A significant increase of H_c of the ion-implanted MnGa with a decrease in the temperature was confirmed by a superconducting quantum interference device magnetometer [21] (data not shown), which also supports the above-described microstructure of the irradiated MnGa, i.e., L1$_0$ MnGa nano-crystals surrounded by the paramagnetic A1 MnGa matrix.
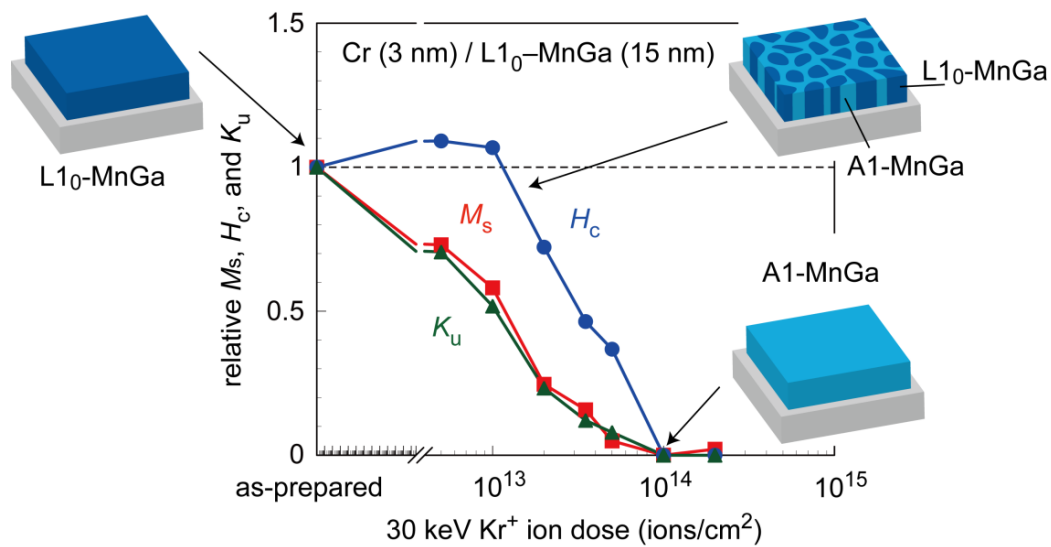

Figure 3. The 30 keV Kr$^+$ ion dose dependence of M_s, H_c, and K_u of MnGa film [20]. These values are normalized as the values of as-prepared MnGa to be 1. The ion dose changes the structure of MnGa from the L1$_0$ phase to the A1 phase, and the microstructure of the L1$_0$ phase surrounded by the A1 phase is expected at ~1 $\times$ 10^{13} ions/cm^2 as shown in the figure [22].
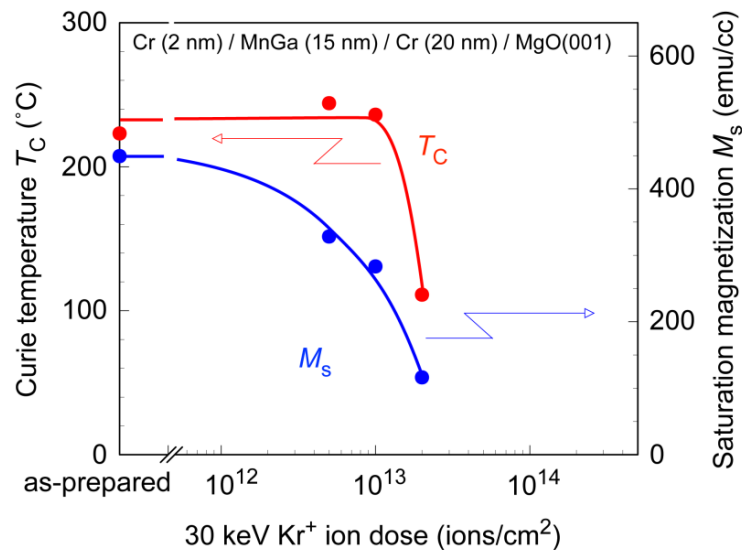

Figure 4. The 30 keV Kr$^+$ ion dose dependence of T_C and M_s of MnGa film.

3. Magnetic Patterning of MnGa and the Switching Field Distribution of Patterned MnGa

Figure 5 provides schematics of the fabrication process of magnetically patterned MnGa films. After the deposition of the $L1_0$-MnGa film, patterned resist (ZEP520A) masks were formed on the film by electron beam lithography (Figure 5a). Then, uniform ion irradiation at a dose of 1×10^{14} ions/cm^2, which completely changes the magnetism of MnGa from ferromagnetic to paramagnetic as shown in Figure 3, was carried out through patterned resist masks (Figure 5b). Finally, the residual resist masks were removed by O$_2$ plasma ashing by using reactive ion etching (Figure 5c).
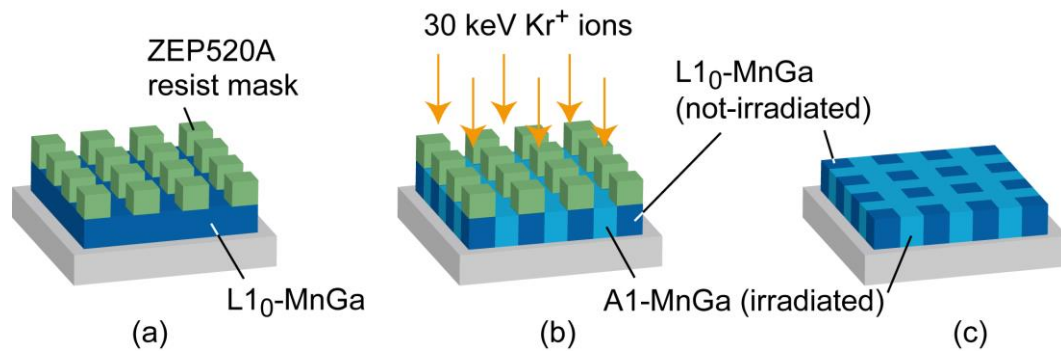

Figure 5. Schematics of the fabrication process of magnetically patterned MnGa films. Square shaped ZEP520A resist masks were fabricated by electron beam lithography (**a**), and the uniform ion irradiation were carried out through resist masks (**b**). Finally, the residual resist masks were removed by plasma ashing (**c**).

Figure 6 shows (a) atomic force microscope (AFM) and (b)–(d) magnetic force microscope (MFM) images of MnGa films patterned by local ion irradiation. The AFM image in Figure 6a was taken for the patterned MnGa with a pitch size of 200 nm. The surface roughness was R_a = 0.36 nm, and there was no topographical structure reflecting the square patterns seen in the MFM images. The MFM images show the domain structure of the patterned MnGa with pitch sizes of (b) 1000 nm, (c) 200 nm, and (d) 80 nm. All of the samples were demagnetized by alternating magnetic field before the MFM measurements. Bright and dark contrasts indicate the magnetization "up" and "down" in the film normal direction, respectively, and the intermediate contrast comes from the paramagnetic MnGa created by the ion irradiation. As seen in Figure 6b–d, bright and dark contrasts were observed in the square-shaped "bit" regions, whereas no magnetic contrast in the "space" regions. The patterned MnGa films have a sufficiently smooth surface with R_a less than 1 nm as shown in Figure 6a, however, the MnGa films have magnetic nanostructure as shown in Figure 6b–d, indicating that planar-patterned BPM are fabricated by the local ion irradiation without flattening processes. Some of the bits exhibit a multi-(maze) domain structure for the patterned MnGa with a pitch size 1000 nm, and the multi-domain structure in the bit was confirmed for the MnGa with a pitch size down to 500 nm (not shown in the figure). Further decrease of the pitch size changes the domain structure in the bit from multi-domain to single domain as shown in Figure 6c,d. Clear magnetic contrasts and sharp transition from up to down magnetization between the adjacent bits were confirmed even in the patterned MnGa with a pitch size of 80 nm as shown in Figure 6d. This indicates the paramagnetic MnGa spaces are effective in suppressing the exchange coupling between the ferromagnetic bits through the spaces, which is the major problem in the Co/Pt and Co/Pd planar BPM [11].

In order to discuss the magnetization process of planar-patterned MnGa, first-order reversal curves (FORCs) [27,28] of the patterned MnGa were measured by AGM and analyzed [29]. Details of the FORC analysis of the planar-patterned MnGa are described in the Ref. [22]. Figure 7 shows the bit size dependence of the average switching field H_{sw} and the switching field distribution $\Delta H_{sw}/H_{sw}$ estimated from the FORC analysis. H_{sw} of the planar-patterned MnGa increased with decreasing the bit size. When the nano-dots in the BPM have a reduced perpendicular anisotropy at the edge (referred to as "bit edge damage"), H_{sw} of the BPM does not increase with decreasing the bit size, since a few

nanometers of the edge damage result in an edge nucleation magnetization reversal [30]. In addition, the exchange coupling between the adjacent bits observed in the planar-patterned Co/Pd also reduces H_{sw} [11]. Therefore, planar-patterned MnGa fabricated by local ion irradiation is expected to have negligibly small bit edge damage as well as negligibly small exchange coupling between the adjacent bits even with a bit size of 40 nm.
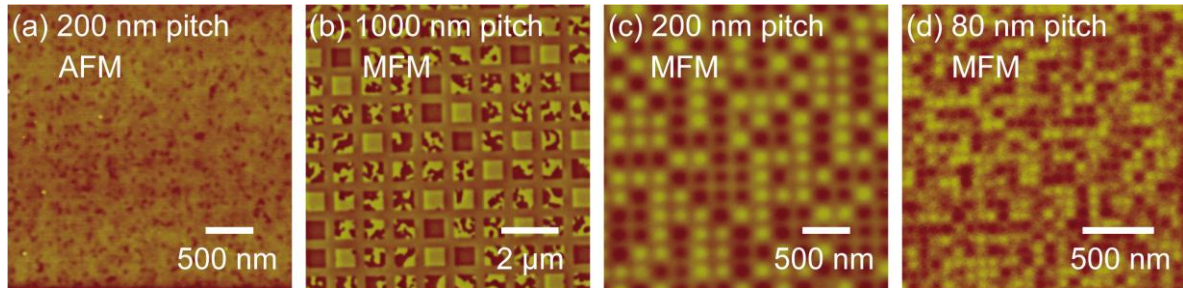

Figure 6. (**a**) AFM images of the planar-pattered MnGa with a pitch size of 200 nm and MFM images of the planar-patterned MnGa with pitch sizes of (**b**) 1000 nm, (**c**) 200 nm, and (**d**) 80 nm [20,22].
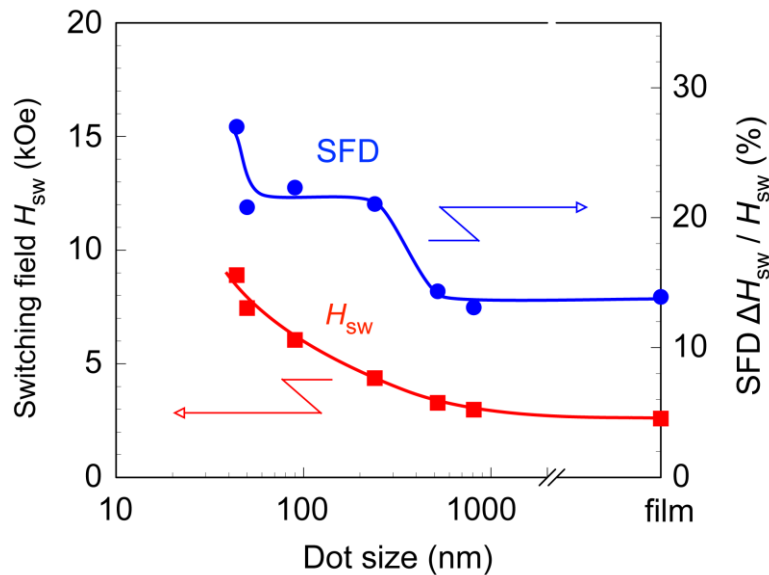

Figure 7. Dot size dependence of H_{sw} and $\Delta H_{sw}/H_{sw}$ estimated from a first-order reversal curve (FORC) analysis of planar-patterned MnGa [22].

The SFD, $\Delta H_{sw}/H_{sw}$, of the un-patterned MnGa film was 13%, and it was almost constant until the bit size was reduced to 500 nm (pitch size of 1000 nm). In these samples, the magnetization reversal process is dominated by nucleation and domain wall propagation. The SFDs in these samples are thought to be determined by the density of the pinning centers existing in the as-prepared MnGa film, which means that the SFD will be decreased by improving the quality of the MnGa films. The SFD increased from 13% to 20% when the bit size became less than 240 nm. We speculate that this increase is related to the transition of the magnetization reversal process from the domain wall propagation to coherent rotation, since the domain structure in the bit changed from a multi-domain structure to a single domain structure at around a bit size of 240 nm (pitch size of 500 nm) as discussed in Figure 6. A further increase of the SFD was observed when the bit size was less than 50 nm. We consider that bit size distribution is the main cause of the increase in the SFD in the small bit size region, as we discussed in detail previously [22]. From these results, optimization of the patterning processes and the quality of the as-prepared film are the key factors to achieve an SFD less than 10%, for the practical application of the MnGa planar BPM.

4. Magnetization Dynamics of Ion-Implanted MnGa

From the FORC analysis discussed in Figure 7, the planar-patterned MnGa is expected to have negligibly small bit edge damage. However, for a more detailed discussion, the anisotropy field of the irradiated MnGa with ion doses around 10^{13} ions/cm^2, which is a transition region from ferromagnetic to paramagnetic as noted in Figure 2, should be investigated. We measured the time resolved magneto-optical Kerr effect (TRMOKE) of the ion-irradiated MnGa films to investigate the anisotropy field and its distribution. A high-power fiber laser with a central wavelength of 1041 nm, a pulse width of 500 fs, and a repetition frequency of 100 kHz was used to obtain the TRMOKE. The frequency-doubled and linearly polarized probe beam was incident normal to the film surface to monitor the perpendicular component of the magnetization after the illumination of the pump beam. The fluences of the pump and probe beams were 0.2 and 0.04 mJ/cm^2, respectively. The external field up to H_{ext} = 14 kOe was applied at an angle of θ_H = 60 deg from the film normal direction. Details of the TRMOKE setup are described in Refs. [31–35]. The sample stack used for the TRMOKE was SiN (5 nm)/MnGa (50 nm)/Cr (10 nm)/MgO(001), and after ion irradiation, an additional SiN (35 nm) layer was deposited to enhance the Kerr rotation of the MnGa. Figure 8 shows the decaying magnetization precessions of the MnGa before and after ion doses of 5×10^{12}, 1×10^{13}, and 2×10^{13} ions/cm^2 under H_{ext} = 14 kOe. The raw data, measured by the TRMOKE, contain the signals of laser-induced demagnetization at the delay time of the probe beam $t = 0$ and exponential decay due to the recovery of the magnetization as described in Ref. [31]. These unnecessary signals were subtracted to extract the decaying precession triggered by the pump illumination as shown in Figure 8. The closed circles and solid lines in Figure 8 indicate the measured data and fitted curves with the damped oscillation function, $A \exp(-t/\tau) \sin\omega t$, respectively, where τ is the relaxation time and ω the angular frequency of the oscillation. A clear oscillation due to the magnetization precession of the as-prepared MnGa can be seen in Figure 8, and the precessions of the MnGa after the ion dose were confirmed to relax faster than those of the MnGa before the ion dose.
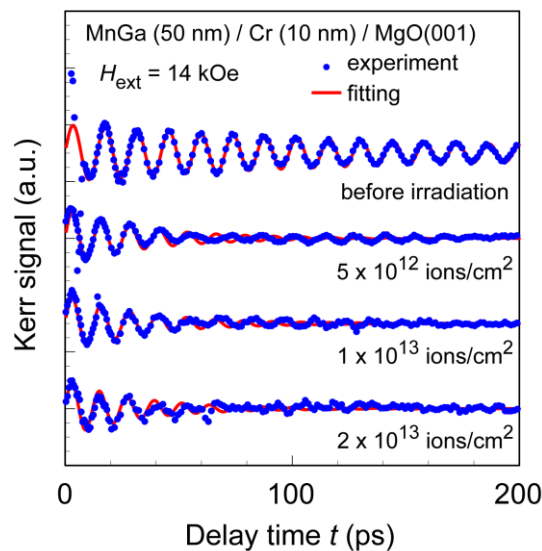

Figure 8. TRMOKE waveforms of MnGa films before and after the ion dose. The ion dose was varied from 5×10^{12} to 2×10^{13} ions/cm^2, and the external field of 14 kOe was applied at θ_H = 60 deg from the film normal direction. Closed circles and solid lines show measured data and fitted curves with damped oscillation function.

The effective anisotropy field H_{keff} and g-factor g were estimated by fitting the H_{ext} dependence of ω shown in Figure 9a with the following expressions [36,37]:

$$\omega = \gamma\sqrt{H_{\theta\theta0}H_{\phi\phi0}} \tag{1a}$$

$$H_{\theta\theta0} = H_{\text{ext}} \cos(\theta_H - \theta) + H_{\text{keff}} \cos^2 \theta \tag{1b}$$

$$H_{\phi\phi0} = H_{\text{ext}} \cos(\theta_H - \theta) + H_{\text{keff}} \cos 2\theta \tag{1c}$$

where $\gamma = \mu_B g/\hbar = 1.105 \times 10^5 g\,[\text{m/A·s}]$ is the gyromagnetic constant, and θ is the stable magnetization angle from the film normal estimated by minimizing the following magnetic energy:

$$E = -M_s H_{\text{ext}} \cos(\theta_H - \theta) + \frac{M_s H_{\text{keff}}}{2} \sin^2 \theta \tag{2}$$

Figure 9b shows the ω dependence of the inverse of the relaxation time $1/\tau$ for the ion-dosed MnGa films. As shown in Figure 9b, $1/\tau$ increased with increasing ω, and the slope for the MnGa without the ion dose is quite small, whereas the slope was found to increase after ion irradiation. $1/\tau$ is influenced by Gilbert damping α, anisotropy distribution ΔH_{keff}, anisotropy axis distribution $\Delta\theta_H$, and two-magnon scattering (TMS) [37–40], and is expressed as,

$$\begin{aligned} \frac{1}{\tau} &= \frac{1}{\tau^{\text{Gilbert}}} + \frac{1}{\tau^{\theta_H}} + \frac{1}{\tau^{H_{\text{keff}}}} + \frac{1}{\tau^{\text{TMS}}} \\ &= \frac{\alpha\gamma}{2}\left(H_{\theta\theta0} + H_{\phi\phi0}\right) + \frac{1}{2}\left|\frac{\partial\omega}{\partial\theta_H}\right|\Delta\theta_H + \frac{1}{2}\left|\frac{\partial\omega}{\partial H_{\text{keff}}}\right|\Delta H_{\text{keff}} + \frac{1}{\tau^{\text{TMS}}}, \end{aligned} \tag{3}$$

if we neglect the contribution from spin pumping [41]. When the TMS and $\Delta\theta_H$ are negligible and $H_{\theta\theta0} \approx H_{\varphi\varphi0}$, Equation (3) is simply expressed as:

$$\frac{1}{\tau} = \alpha\omega + \frac{1}{2}\left|\frac{\partial\omega}{\partial H_{\text{keff}}}\right|\Delta H_{\text{keff}} \tag{4}$$

indicating that $1/\tau$ is roughly proportional to α [37]. From the data in Figure 9b, the slope and *y*-intercept for the MnGa without the ion dose are estimated to be 0.01 and 1.3 Grad/s, respectively, suggesting small α ~0.01 and ΔH_{keff} ~150 Oe. The TMS contribution is calculated as [38–40]:

$$\frac{1}{\tau^{\text{TMS}}} = N_0 \int \frac{C(k)}{\omega} \text{Im}\left(\frac{1}{\omega_{\mathbf{k}}^2 - \omega^2 + i\omega\delta\omega_{\mathbf{k}}}\right) d\mathbf{k} \tag{5}$$

where $\mathbf{k}$ is the magnon wave vector, k its amplitude, N_0 the scattering intensity, $C(k)$ the correlation function, $\omega_{\mathbf{k}}$ the spin wave dispersion, and $\delta\omega_{\mathbf{k}}$ the inverse lifetime of the spin wave. These are expressed as [38,39]:

$$N_0 = \gamma^4\left(4H_{\theta\theta0}^2 \cos^4\theta + 4H_{\phi\phi0}^2 \cos^2 2\theta - 8H_{\theta\theta0}H_{\phi\phi0}\cos^2\theta\cos 2\theta\right)\Delta H_{\text{keff}}^2 \tag{6}$$

$$C(k) = \frac{2\pi\xi^2}{\left(1 + (k\xi)^2\right)^{3/2}} \tag{7}$$

$$\omega_{\mathbf{k}} = \gamma\sqrt{H_{\theta\theta}(\mathbf{k})H_{\phi\phi}(\mathbf{k})} \tag{8}$$

$$\delta\omega_{\mathbf{k}} = \alpha\gamma\left(H_{\theta\theta}(\mathbf{k}) + H_{\phi\phi}(\mathbf{k})\right) \tag{9}$$

where ξ is the correlation length, and $H_{\theta\theta}(\mathbf{k})$ and $H_{\varphi\varphi}(\mathbf{k})$ are given by [38]:

$$H_{\theta\theta}(\mathbf{k}) = H_{\theta\theta0} + \frac{M_s}{\mu_0}(1 - N_k)\cos^2\phi_k + \frac{2A_{\text{ex}}}{M_s}k^2 \tag{10a}$$

$$H_{\phi\phi}(\mathbf{k}) = H_{\phi\phi0} - \frac{M_s}{\mu_0}(1 - N_k)\sin^2\phi_k + \frac{2A_{\text{ex}}}{M_s}k^2 \tag{10b}$$

where μ_0 is the permeability of vacuum, A_{ex} the exchange stiffness, and φ_k the azimuth angle of the spin wave. N_k is the wave number dependent demagnetizing factor which is given by [38]:

$$N_k = \frac{1 - e^{-kd}}{kd} \qquad (11)$$

where d is the film thickness. $1/\tau^{TMS}$ increases with increasing ω; i.e., it increases the slope in Figure 9b, since the increase of H_{ext} increases θ. From Equations (5) and (6), $1/\tau^{TMS}$ is proportional to $\Delta H_{keff}{}^2$, and thus the increase of ΔH_{keff} results in the increases of the slope of the curve of $1/\tau$ vs. ω. The increase of ΔH_{keff} also increases the y-intercept of Figure 9b from Equation (4). In Figure 9b, the solid lines show fitted curves with Equation (3), where we assumed $\Delta \theta_H = 0$, since the second term in Equation (3) for the MnGa without ion irradiation was negligibly small, and the second term is considered not to increase after ion irradiation. We also assumed that the Gilbert damping stayed constant after ion irradiation, since the ion irradiation will not contribute to an increase in the intrinsic damping.
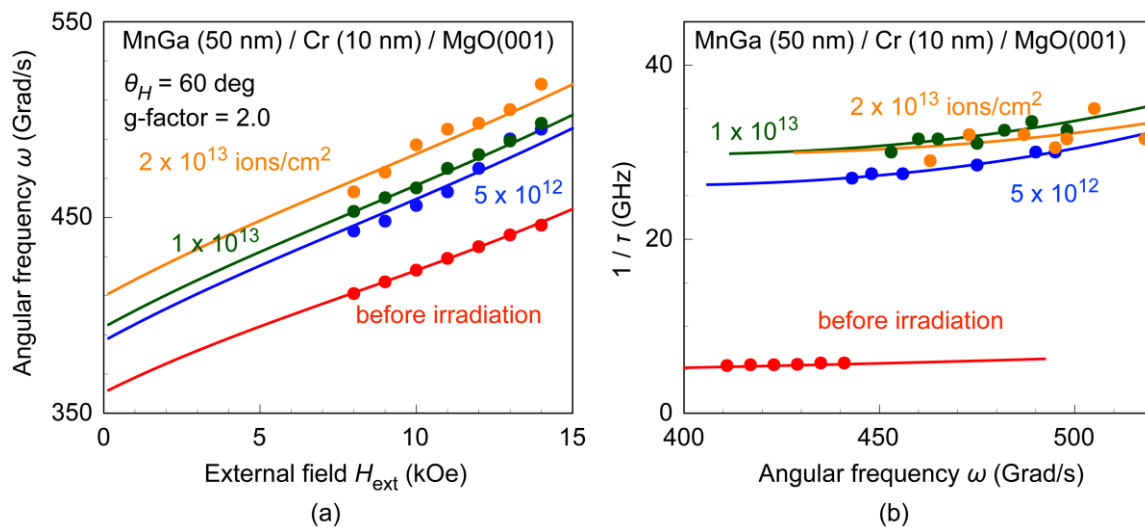

Figure 9. (**a**) H_{ext} dependence of ω and (**b**) ω dependence of $1/\tau$ obtained by fitting the TRMOKE waveforms of MnGa films before and after the ion dose. The ion dose was varied from 5×10^{12} to 2×10^{13} ions/cm^2, and the external field was applied at $\theta_H = 60$ deg from the film normal direction. Solid lines in (**a**,**b**) show fitted curves with Equations (1) and (3), respectively.

Figure 10 shows the ion dose dependence of H_{keff}, ΔH_{keff}, α, and ξ of the ion-irradiated MnGa films. The g-factor of all MnGa films was estimated to be 2.0 irrespective of ion implantation. α of the as-prepared MnGa is estimated to be 0.008, which is consistent with the previous result [42]. H_{keff} of the MnGa before the irradiation was 20 kOe, which roughly agrees with that estimated from *M–H* loops shown in Figure 1. H_{keff} increased after the ion dose and stayed constant at H_{keff} ~23 kOe. This suggests that the ion irradiation does not cause the reduction of the average value of the anisotropy, which is in accordance with the small bit edge damage in the patterned MnGa. On the other hand, ΔH_{keff} significantly increased from 0.2 kOe to 3 kOe with an increase in the ion dose. Accordingly, ξ decreased from 10 nm to 3 nm after the ion irradiation. These trends are explained by the microstructure discussed in Figures 2 and 3. After the ion irradiation, L1$_0$ MnGa nano-crystals are expected to be surrounded by the paramagnetic A1 MnGa matrix. This results in a large distribution of the effective field acting in the nano-crystals, since each L1$_0$-MnGa nano-crystal has different shape anisotropy. For the thin-film MnGa, the demagnetizing field is estimated to be 7.5 kOe, whereas the demagnetizing field of an isolated MnGa nano-crystal with an aspect ratio of 1 will be 2.5 kOe. The microstructure also explains the reduction of ξ by the ion irradiation. ξ corresponds to the length of disorder in the film, and ξ ~10 nm for an as-prepared MnGa film is thought to be related to the grain size of the MnGa, which is expected to be a few tens of nanometers from the AFM image in Figure 6a.

After ion irradiation, ξ will be reduced by the ion irradiation. The ion dose of 1×10^{13} ions/cm^2 corresponds to 1 ion per 3 nm $\times$ 3 nm, which agrees well with ξ after ion irradiation.
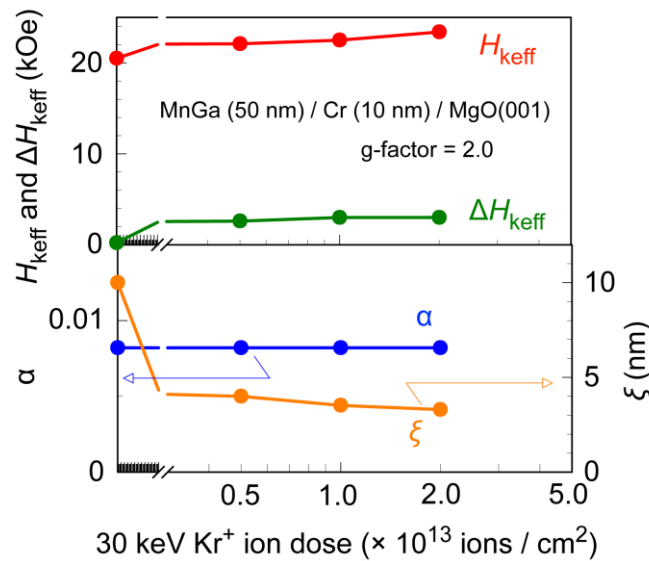

Figure 10. The 30 keV Kr$^+$ ion dose dependence of H_{keff}, ΔH_{keff}, α, and ξ of the MnGa films before and after ion irradiation. These values were obtained by fitting with Equations (1) and (3).

5. Conclusions

We summarized the variation of the magnetic properties of MnGa films with ion irradiation, and reported the magnetic patterning and the SFD of MnGa fabricated by local ion irradiation. We also investigated the magnetization dynamics of irradiated MnGa films to study the origin of the SFD. The (001)-oriented L1$_0$-MnGa films grown on the Cr-buffered MgO(001) substrate exhibited strong perpendicular anisotropy, and the magnetization and perpendicular anisotropy of the MnGa were eliminated by a Kr$^+$ ion dose of 1×10^{14} ions/cm^2. The ion irradiation changes the crystal structure of MnGa from the ferromagnetic L1$_0$ phase to the paramagnetic A1 phase. The microstructure of MnGa after the ion dose of $\sim 10^{13}$ ions/cm^2 is expected to be a mixture of the ferromagnetic L1$_0$-MnGa and paramagnetic A1-MnGa.

Uniform ion implantation through patterned resist masks is effective in producing topographically flat and magnetically patterned MnGa, i.e., planar-patterned MnGa. We confirmed 40 nm $\times$ 40 nm magnetic bits on the MnGa patterned by this technique. The average switching field H_{sw} of the planar-patterned MnGa increased with decreasing the bit size, indicating the negligible bit edge damage in the patterned MnGa. However, the planar-patterned MnGa exhibits a rather large SFD of 25% for a bit size of ~ 40 nm. The improvement of the film quality, e.g., reduction of the density of the pinning centers, and the optimization of the patterning processes to reduce the bit size distribution will reduce the SFD.

Using the TRMOKE measurements, we evaluated the average anisotropy field H_{keff}, its distribution ΔH_{keff}, the Gilbert damping α, and the length of disorder ξ. MnGa before ion irradiation exhibits large $H_{\mathrm{keff}} = 20$ kOe, small $\Delta H_{\mathrm{keff}} = 200$ Oe, and small $\alpha = 0.008$. The MnGa films after the ion doses from 5×10^{12} to 2×10^{13} ions/cm^2 exhibited larger H_{keff} of 22~23 kOe than that of the as-prepared MnGa. This suggests that the perpendicular anisotropy was not decreased by the ion dose, resulting in the small bit edge damage in the planar-patterned MnGa films. With the ion irradiation, ΔH_{keff} increased from 0.2 kOe to 3 kOe, whereas ξ decreased from 10 nm to 3 nm. These are explained by the model of the microstructure comprised of the ferromagnetic L1$_0$-MnGa and paramagnetic A1-MnGa, since the demagnetizing field and the length of disorder are expected to reduce significantly in the isolated L1$_0$-MnGa nano-crystal surrounded by paramagnetic A1-MnGa compared to the continuous L1$_0$-MnGa film.

Conflicts of Interest: The authors declare no conflict of interest.

References

1. White, R.L.; New, R.M.H.; Fabian, R.; Pease, W. Patterned media: A viable route to 50 Gbit/in^2 and up for magnetic recording? *IEEE Trans. Magn.* **1997**, *33*, 990–995. [CrossRef]

2. Terris, B.D. Fabrication challenges for patterned recording media. *J. Magn. Magn. Mater.* **2009**, *321*, 512–517. [CrossRef]

3. Kikitsu, A. Prospects for bit patterned media for high-density magnetic recording. *J. Magn. Magn. Mater.* **2009**, *321*, 526–530. [CrossRef]

4. Charap, S.H.; Lu, P.-L.; He, Y. Thermal stability of recorded information at high densities. *IEEE Trans. Magn.* **1997**, *33*, 978–983. [CrossRef]

5. Wood, R. The feasibility of magnetic recording at 1 terabit per square inch. *IEEE Trans. Magn.* **2000**, *36*, 36–42. [CrossRef]

6. Choi, C.; Yoon, Y.; Hong, D.; Oh, Y.; Talke, F.E.; Jin, S. Planarization of patterned magnetic recording media to enable head flyability. *Microsyst. Technol.* **2011**, *17*, 395–402. [CrossRef]

7. Chappert, C.; Bernas, H.; Ferré, J.; Kottler, V.; Jamet, J.-P.; Chen, Y.; Cambril, E.; Devolder, T.; Rousseaux, F.; Mathet, V.; Launois, H. Planar patterned magnetic media obtained by ion irradiation. *Science* **1998**, *280*, 1919–1922. [CrossRef]

8. Ferré, J.; Chappert, C.; Bernas, H.; Jamet, J.-P.; Meyer, P.; Kaitasov, O.; Lemerle, S.; Mathet, V.; Rousseaux, F.; Launois, H. Irradiation induced effects on magnetic properties of Pt/Co/Pt ultrathin films. *J. Magn. Magn. Mater.* **1999**, *198–199*, 191–193.

9. Hyndman, R.; Warin, P.; Gierak, J.; Ferré, J.; Chapman, J.N.; Jamet, J.-P.; Mathet, V.; Chappert, C. Modification of Co/Pt multilayers by gallium irradiation—Part 1: The effect on structural and magnetic properties. *J. Appl. Phys.* **2001**, *90*, 2843–3849. [CrossRef]

10. Suharyadi, E.; Natsume, S.; Kato, T.; Tsunashima, S.; Iwata, S. Microstructure and magnetic properties of the FIB irradiated Co/Pd multilayer films. *IEEE Trans. Magn.* **2005**, *41*, 3595–3597. [CrossRef]

11. Suharyadi, E.; Kato, T.; Tsunashima, S.; Iwata, S. Magnetic Properties of Patterned Co/Pd Nanostructures by E-Beam Lithography and Ga Ion Irradiation. *IEEE Trans. Magn.* **2006**, *42*, 2972–2974. [CrossRef]

12. Hinoue, T.; Ito, K.; Hirayama, Y.; Hosoe, Y. Effects of lateral straggling of ions on patterned media fabricated by nitrogen ion implantation. *J. Appl. Phys.* **2012**, *111*, 07B912. [CrossRef]

13. Gaur, N.; Kundu, S.; Piramanayagam, S.N.; Maurer, S.L.; Tan, H.K.; Wong, S.K.; Steen, S.E.; Yang, H.; Bhatia, C.S. Lateral displacement induced disorder in L1$_0$-FePt nanostructures by ion-implantation. *Sci. Rep.* **2013**, *3*, 1907. [CrossRef]

14. Fassbender, J.; Liedke, M.O.; Strache, T.; Möller, W.; Menéndez, E.; Sort, J.; Rao, K.V.; Deevi, S.C.; Nogués, J. Ion mass dependence of irradiation-induced local creation of ferromagnetism in Fe$_{60}$Al$_{40}$ alloys. *Phys. Rev. B* **2008**, *77*, 174430. [CrossRef]

15. Kato, T.; Iwata, S.; Yamauchi, Y.; Tsunashima, S.; Matsumoto, K.; Morikawa, T.; Ozaki, K. Planar patterned media fabricated by ion irradiation into $CrPt_3$ ordered alloy films. *J. Appl. Phys.* **2009**, *105*, 07C117. [CrossRef]

16. Kato, T.; Iwata, S.; Yamauchi, Y.; Tsunashima, S. Modification of magnetic properties and structure of Kr^+ ion-irradiated $CrPt_3$ films for planar bit patterned media. *J. Appl. Phys.* **2009**, *106*, 053908. [CrossRef]

17. Suharyadi, E.; Oshima, D.; Kato, T.; Iwata, S. Switching field distribution of planar-patterned $CrPt_3$ nanodots fabricated by ion irradiation. *J. Appl. Phys.* **2011**, *109*, 07B771. [CrossRef]

18. Oshima, D.; Suharyadi, E.; Kato, T.; Iwata, S. Observation of ferri-nonmagnetic boundary in $CrPt_3$ line-and-space patterned media using a dark-field transmission electron microscope. *J. Magn. Magn. Mater.* **2012**, *324*, 1617–1621. [CrossRef]

19. Oshima, D.; Tanimoto, M.; Kato, T.; Fujiwara, Y.; Nakamura, T.; Kotani, Y.; Tsunashima, S.; Iwata, S. Modifications of Structure and Magnetic Properties of $L1_0$ MnAl and MnGa Films by Kr^+ Ion Irradiation. *IEEE Trans. Magn.* **2014**, *50*, 3203407. [CrossRef]

20. Oshima, D.; Kato, T.; Iwata, S.; Tsunashima, S. Control of Magnetic Properties of MnGa films by Kr^+ Ion Irradiation for Application to Bit Patterned Media. *IEEE Trans. Magn.* **2013**, *49*, 3608–3611. [CrossRef]

21. Oshima, D.; Tanimoto, M.; Kato, T.; Fujiwara, Y.; Nakamura, T.; Kotani, Y.; Tsunashima, S.; Iwata, S. Ion Irradiation-Induced Magnetic Transition of MnGa Alloy Films Studied by X-Ray Magnetic Circular Dichroism and Low-Temperature Hysteresis Loops. *IEEE Trans. Magn.* **2016**, *52*, 3201804. [CrossRef]

22. Oshima, D.; Kato, T.; Iwata, S. Switching field distribution of MnGa bit patterned film fabricated by ion beam irradiation. *IEEE Trans. Magn.* **2018**, *54*, 3200207. [CrossRef]

23. Xu, Q.; Kanbara, R.; Kato, T.; Iwata, S.; Tsunashima, S. Control of magnetic properties of MnBi and MnBiCu thin films by Kr^+ ion irradiation. *J. Appl. Phys.* **2012**, *111*, 07B906. [CrossRef]

24. Mizukami, S.; Kubota, T.; Wu, F.; Zhang, X.; Miyazaki, T.; Naganuma, H.; Oogane, M.; Sakuma, A.; Ando, Y. Composition dependence of magnetic properties in perpendicularly magnetized epitaxial thin films of Mn-Ga alloys. *Phys. Rev. B* **2012**, *85*, 014416. [CrossRef]

25. Carr, W.J. Temperature dependence of ferromagnetic anisotropy. *Phys. Rev.* **1958**, *109*, 1971–1976. [CrossRef]

26. Okamoto, S.; Kikuchi, N.; Kitakami, O.; Miyazaki, T.; Shimada, Y.; Fukamichi, K. Chemical-order-dependent magnetic anisotropy and exchange stiffness constant of FePt (001) epitaxial films. *Phys. Rev. B* **2002**, *66*, 024413. [CrossRef]

27. Mayergoyz, I.D.; Friedman, G. Generalized Preisach model of hysteresis. *IEEE Trans. Magn.* **1988**, *24*, 212–217. [CrossRef]

28. Pike, C.R.; Roberts, A.P.; Verosub, K.L. Characterizing interactions in fine magnetic particle systems using first order reversal curves. *J. Appl. Phys.* **1999**, *85*, 6660–6667. [CrossRef]

29. Egli, R. VARIFORC: An optimized protocol for calculating non-regular first-order reversal curve (FORC) diagrams. *Glob. Planet. Chang.* **2013**, *110*, 302–320. [CrossRef]

30. Shaw, J.M.; Russek, S.E.; Thomson, T.; Donahue, M.J.; Terris, B.D.; Hellwig, O.; Dobisz, E.; Schneider, M.L. Reversal mechanisms in perpendicular magnetized nanostructures. *Phys. Rev. B* **2008**, *78*, 024414. [CrossRef]

31. Kato, T.; Nakazawa, K.; Komiya, R.; Nishizawa, N.; Tsunashima, S.; Iwata, S. Compositional dependence of g-factor and damping constant of GdFeCo amorphous alloy films. *IEEE Trans. Magn.* **2008**, *44*, 3380–3383. [CrossRef]

32. Kato, T.; Matsumoto, Y.; Okamoto, S.; Kikuchi, N.; Kitakami, O.; Nishizawa, N.; Tsunashima, S.; Iwata, S. Time-resolved magnetization dynamics and damping constant of sputtered Co/Ni multilayers. *IEEE Trans. Magn.* **2011**, *47*, 3036–3039. [CrossRef]

33. Kato, T.; Matsumoto, Y.; Kashima, S.; Okamoto, S.; Kikuchi, N.; Iwata, S.; Kitakami, O.; Tsunashima, S. Perpendicular anisotropy and Gilbert damping in Sputtered Co/Pd multilayers. *IEEE Trans. Magn.* **2012**, *48*, 3288–3291. [CrossRef]

34. Higashide, T.; Dai, B.; Kato, T.; Oshima, D.; Iwata, S. Effective damping constant and current induced magnetization switching of GdFeCo/TbFe exchange-coupled bilayers. *IEEE Mang. Lett.* **2016**, *7*, 3505605. [CrossRef]

35. Kimura, T.; Dong, X.; Adachi, K.; Oshima, D.; Kato, T.; Sonobe, Y.; Okamoto, S.; Kikuchi, N.; Kawato, Y.; Kitakami, O.; et al. Spin transfer torque switching of Co/Pd multilayers and Gilbert damping of Co-based multilayers. *Jpn. J. Appl. Phys.* **2018**, *57*, 09TD01. [CrossRef]

36. Suhl, H. Ferromagnetic resonance in nickel ferrite between one and two kilomegacycles. *Phys. Rev.* **1955**, *97*, 555–557. [CrossRef]

37. Beaujour, J.-M.; Ravelosona, D.; Tudosa, I.; Fullerton, E.E.; Kent, A.D. Ferromagnetic resonance linewidth in ultrathin films with perpendicular magnetic anisotropy. *Phys. Rev. B* **2009**, *80*, 180415(R). [CrossRef]

38. McMichael, R.D.; Krivosik, P. Classical Model of Extrinsic Ferromagnetic Resonance Linewidth in Ultrathin Films. *IEEE Trans. Magn.* **2004**, *40*, 2–11. [CrossRef]

39. Landeros, P.; Arias, R.E.; Mills, D.L. Two magnon scattering in ultrathin ferromagnets: The case where the magnetization is out of plane. *Phys. Rev. B* **2008**, *77*, 214405. [CrossRef]

40. Iihama, S.; Sakuma, A.; Naganuma, H.; Oogane, M.; Mizukami, S.; Ando, Y. Influence of L10 order parameter on Gilbert damping constants for FePd thin films investigated by means of time-resolved magneto-optical Kerr effect. *Phys. Rev. B* **2016**, *94*, 174425. [CrossRef]

41. Tserkovnyak, Y.; Brataas, A.; Bauer, G.E.W. Enhanced Gilbert damping in thin ferromagnetic films. *Phys. Rev. Lett.* **2002**, *88*, 117601. [CrossRef] [PubMed]

42. Mizukami, S.; Wu, F.; Sakuma, A.; Walowski, J.; Watanabe, D.; Kubota, T.; Zhang, X.; Naganuma, H.; Oogane, M.; Ando, Y.; et al. Long-lived ultrafast spin precession in manganese alloys films with a large perpendicular magnetic anisotropy. *Phys. Rev. Lett.* **2011**, *106*, 117201. [CrossRef] [PubMed]